Key Points:
- A 62-year ground-based magnetic data set from the Tatuoca Observatory (northern Brazil) was recovered, processed, and analyzed
- Data and TIEGCM model indicate geomagnetic daily variation changing from a low-latitude type to an equatorial type due to secular variation
- Long-term changes in the seasonal, day-to-day, and lunar variations and in the equatorial counter electrojet are revealed

Evolution of the Geomagnetic Daily Variation at Tatuoca, Brazil, From 1957 to 2019: A Transition From Sq to EEJ

G. Soares[1,2] , Y. Yamazaki[2] , I. Cnossen[3] , J. Matzka[2] , K. J. Pinheiro[1] , A. Morschhauser[2] , P. Alken[4,5] , and C. Stolle[2,6]

[1]Observatório Nacional, Rio de Janeiro, Brazil, [2]GFZ German Research Centre for Geosciences, Potsdam, Germany, [3]British Antarctic Survey, Cambridge, UK, [4]Cooperative Institute for Research in Environmental Sciences, University of Colorado Boulder, Boulder, CO, USA, [5]National Centers for Environmental Information, NOAA, Boulder, CO, USA, [6]Faculty of Science, University of Potsdam, Potsdam, Germany

Abstract The magnetic equator in the Brazilian region has moved over 1,100 km northward since 1957, passing the geomagnetic observatory Tatuoca (TTB), in northern Brazil, around 2013. We recovered and processed TTB hourly mean values of the geomagnetic field horizontal (H) component from 1957 until 2019, allowing the investigation of long-term changes in the daily variation due to the influence of secular variation, solar activity, season, and lunar phase. The H day-to-day variability and the occurrence of the counter electrojet at TTB were also investigated. Until the 1990s, ionospheric solar quiet currents dominated the quiet-time daily variation at TTB. After 2000, the magnitude of the daily variation became appreciably greater due to the equatorial electrojet (EEJ) contribution. The H seasonal and day-to-day variability increased as the magnetic equator approached, but their amplitudes normalized to the average daily variation remained at similar levels. Meanwhile, the amplitude of the lunar variation, normalized in the same way, increased from 5% to 12%. Within the EEJ region, the occurrence rate of the morning counter electrojet (MCEJ) increased with proximity to the magnetic equator, while the afternoon counter electrojet (ACEJ) did not. EEJ currents derived from CHAMP and Swarm satellite data revealed that the MCEJ rate varies with magnetic latitude within the EEJ region while the ACEJ rate is largely constant. Simulations with the Thermosphere-Ionosphere-Electrodynamics General Circulation Model based on different geomagnetic main field configurations suggest that long-term changes in the geomagnetic daily variation at TTB can be attributed to the main field secular variation.

1. Introduction

The South Atlantic Anomaly is a region characterized by comparatively weak geomagnetic field strength with strong westerly declination and a strong bending of the magnetic equator. The Tatuoca geomagnetic observatory in Brazil (TTB, 1.2°S, 48.5°W) is located within this region and experiences a change of geomagnetic inclination of 0.4° per year (Thébault et al., 2015). Since the ionospheric dynamo currents are theoretically predicted to change with the Earth's main field, the behavior of the geomagnetic daily variation in Brazil may also change over time due to the influence of the secular variation.

At low latitudes and in equatorial regions, the regular geomagnetic daily variation is mainly driven by the ionospheric solar quiet (Sq) and equatorial electrojet (EEJ) currents (Yamazaki & Maute, 2017). Both Sq and EEJ currents are controlled by ionospheric conductivities, which depend on the plasma density and on the intensity of the geomagnetic main field (Cnossen, 2017; Takeda, 1996). The current density of the EEJ is on the order of 10^{-6} A/m^2, which is typically one order of magnitude greater than the low-latitude Sq currents (Onwumechili, 1997). The EEJ usually flows eastward within ±3° latitude around the magnetic equator, where a strong zonal Hall current results from the horizontal geomagnetic field. It is accompanied by return currents, which flow at low latitudes (3–9° away from the magnetic equator) in the opposite direction and with lower strength compared to the EEJ (Onwumechili, 1992; Zhou et al., 2018). The eastward flow of the EEJ is sometimes observed to reverse westward, giving rise to the so-called equatorial counter electrojet (CEJ), a phenomenon that mainly depends on the variability of the atmospheric tides and its effects on the global wind system (Gouin, 1962; Gurubaran, 2002; Hanuise et al., 1983; Marriott et al., 1979; Mayaud, 1977; Soares et al., 2019; Zhou et al., 2018).

Geomagnetic records from Brazil can provide valuable insight into the main field influence on the ionospheric currents, as it is a region of strong secular variation (Hartmann & Pacca, 2009). The first attempt to measure the EEJ magnetic field in the Brazilian sector dates back to March 1952, when a 13-day field campaign at the Island of Fernando de Noronha (3.9°S, 32.4°W, northeast Brazil, QD latitude was −0.6°) gave an average H-component daily range of 127 nT (Gama, 1953). Later, Gama (1972) described the average daily variation in Brazil from low-latitude and equatorial stations. Hesse (1982) focused on the investigation of the EEJ in the Brazilian sector, using a dedicated chain of nine temporary stations and the geomagnetic observatories Vassouras (22.4°S, 43.6°W) and Paramaribo (5.8°N, 55.2°W). Rigoti et al. (1999) used data from 16 selected quiet days from a temporary array of 29 vector magnetometers to model the EEJ in N-NE Brazil, inverting parameters such as current intensity, width, and center.

More recent studies on the daily variation in the Brazilian sector were mostly based on relatively short data sets (Bolzan et al., 2018; Rastogi et al., 2010; Rastogi & Trivedi, 2009; Rastogi & Yumoto, 2006; Shume et al., 2010; Yizengaw et al., 2014). Moro et al. (2016) studied E-region electric field variability at the dip equator from 2001 to 2010 over Brazil and Peru by means of backscatter radar data. They indicated that the geomagnetic field secular variation significantly affects the measurements from the Brazilian sector. Recently, a 10-year long data set from TTB was used for the first time in a study on the occurrence of CEJ events (Soares et al., 2018). Here we further extend the TTB data back to the 1950s to investigate long-term changes in the geomagnetic daily variation associated with Sq and EEJ.

At a given longitude sector, Sq and EEJ magnetic signals are usually separated using measurements from a meridional (north-south) chain of stations crossing the magnetic equator (e.g., Yamazaki et al., 2010). Such a chain can measure equatorial and low-latitude ionospheric currents at the same time and allows for the investigation of individual geomagnetic events. With a single station like TTB, only a statistical analysis is possible, for instance by comparing annual means for years when the distance to the magnetic equator was large with annual means for years when this distance was small. On the other hand, using a single station with a long time series offers additional advantages: it allows the investigation of the field dependence on the magnetic equator distance at high resolution in geomagnetic latitude (as opposed to a sparse magnetometer chain) and with full local time and seasonal coverage (as opposed to satellites, which would need several years to reach full local time and seasonal coverage).

In this work, we show how and when the characteristics of the geomagnetic daily variation at TTB changed from the low-latitude "Sq type" to the equatorial "EEJ type." For this purpose, we use TTB horizontal (H) component records and examine long-term changes in its daily range, solar flux dependence, seasonal variation, day-to-day variability, lunar variation, and CEJ occurrence rate. The H component was chosen because it contains most of the signal that we are interested in (low-latitude Sq and EEJ) when compared to other geomagnetic components. We also analyze geomagnetic data from CHAMP and Swarm satellites to better understand the effects of the EEJ currents on TTB data. Lastly, we investigate the link between long-term changes in the daily variation at TTB and the secular variation of the main field using simulations with the Thermosphere-Ionosphere-Electrodynamics General Circulation Model (TIEGCM). The simulations allow us to isolate the effects of magnetic field changes from other potential sources of long-term change that are not taken into account in our simulations, such as variations in solar activity, which affects Sq and EEJ variations primarily via its effect on ionospheric conductivity (e.g., Rastogi & Iyer, 1976; Takeda, 2013; Yamazaki et al., 2011), or whole-atmosphere anthropogenic climate change (e.g., Marsh et al., 2013), which could potentially affect ionospheric current systems via changes in upwardly propagating tides (Yamazaki & Kosch, 2014). Comparisons between modeled and observed long-term changes in the daily variation at TTB are used to check whether the secular variation in the main field is primarily responsible for the observed long-term changes or if other sources have played a role as well.

2. Data and Model

2.1. Tatuoca Geomagnetic Observatory

TTB observatory was installed in 1957 by Observatório Nacional on the Tatuoca Island (in the Amazon River, close to Belém, Brazil) and has been operating since then (Gama, 1958). Since 2015, TTB is operated in cooperation with the GFZ German Research Centre for Geosciences (Morschhauser et al., 2017). During the Second International Polar Year, a temporary magnetic station was established and operated on Tatuoca
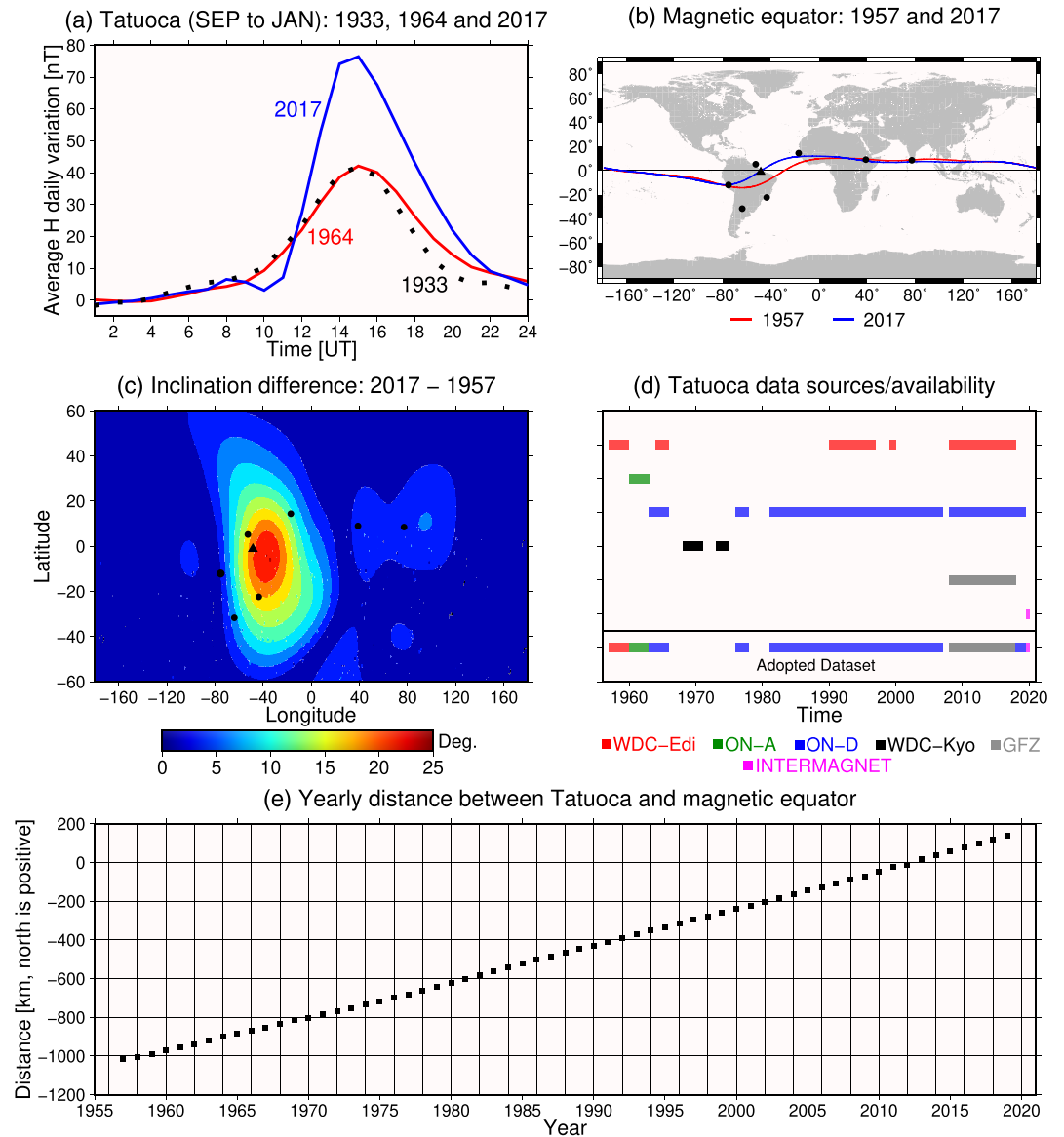
Figure 1. (a) Average H-component daily variation at Tatuoca for quiet days in the period from September to January for 1933 (black dots), 1964 (red line), and 2017 (blue line). (b) Map of selected equatorial and South American geomagnetic observatories with long time series. From west to east: HUA, PIL, KOU, TTB (highlighted as a black triangle), VSS, MBO, AAE, and TRD. The magnetic equator for 1957 (red) and 2017 (blue) is also shown. (c) Inclination change from 1957 to 2017 and observatories as in panel (b). (d) TTB H-component data availability versus time and its sources: WDC-Edi (WDC Edinburgh, digital), ON-A (Observatório Nacional, analogue), ON-D (Observatório Nacional, digital), WDC-Kyo (WDC Kyoto, analogue, not used here), GFZ (GFZ Data Services, digital), and INTERMAGNET (digital). (e) Yearly distance between TTB and the magnetic equator from 1957 to 2019.

Island from September 1933 to January 1934 (Olsen, 1951). Figure 1a shows the average H component daily variation of 1933, 1964, and 2017 (solar minimum years) for September to January periods in Tatuoca, considering only the five quietest days of each month. A typical low-latitude H-component daily variation (i.e., H variation with nighttime values subtracted) is observed for 1933 (black dots) and 1964 (red line), with peak values of about 40 nT. The daily variation in 2017 (blue line) is significantly different and its noon-time range is almost two times larger.

The different patterns of the H-component daily variation observed for 1933, 1964, and 2017 may be explained by the changing geomagnetic latitudes of TTB due to the fast northward movement of the magnetic equator (an average of about 19 km/year since 1957, according to the International Geomagnetic

Reference Field, IGRF-12, Thébault et al., 2015). Figure 1b shows the location of TTB (black triangle) and other low-latitude geomagnetic observatories with long time series (black circles) as well as the position of the magnetic equator for 1957 and 2017, which distinctively changed in the Brazilian sector. Indeed, Figure 1c shows that TTB is placed in the area of maximum difference in inclination values from 1957 to 2017 (nearly 25°, according to IGRF). Significant inclination changes can also be observed for the low-latitude stations KOU, VSS, and MBO, but not for the other equatorial geomagnetic observatories HUA (see, e.g., Matzka et al., 2017), AAE, and TRD. Details on the impact of long-term changes of the geomagnetic core field strength and geometry on external fields are discussed in the review by Cnossen (2017).

In this work, we used hourly mean values of the geomagnetic field H-component measured at TTB from 1957 to 2019. Figure 1d shows the availability of TTB data and the corresponding data sources: WDC-Edi (WDC Edinburgh, digital data available at http://www.wdc.bgs.ac.uk/), ON-A (Observatório Nacional analogue data in Gama, 1964), ON-D (Observatório Nacional, previously unpublished digital data from the observatory archives), GFZ (GFZ Data Services, Soares, Yamazaki, et al., 2018), and INTERMAGNET (International Real-time Magnetic Observatory Network, www.intermagnet.org). This leads to a combined data set of 49 years, while 14 years are still missing, mostly in the 1960s and 1970s, but also in 2007. A further potential source of TTB data to fill in these gaps, but still requiring digitalization, are the magnetogram images available from WDC Kyoto at http://wdc.kugi.kyoto-u.ac.jp/film/index.html (labeled WDC-Kyo in Figure 1d) and from the Observatório Nacional analogue archives. The final data set, adopted in this work, is shown in the lower portion of Figure 1d. Additionally, Figure 1e shows the yearly distance between TTB and the magnetic equator from 1957 to 2019, according to IGRF-12. The magnetic equator moved 1,155 km in 62 years with a nearly constant rate of change of 19 km/year, crossing TTB around 2013.

The combined data set was processed before data analysis. A total of 237 spikes that could not be explained by geomagnetic field variations was deleted from the data set, 36 obvious typographic errors and 14 periods with unrealistic offsets were corrected. Time stamps had to be converted from local time to universal time in the TTB records until 1999. In addition, ON-D data from 2004 to 2006 were available only as raw variation data in units of millimeters as measured from photographic paper, which was used as the recording medium in a classical variometer system. In this case, data were calibrated by converting from millimeter to nanotesla (by using available scale value tables) and adding baseline values to the variation data in order to obtain absolute values of the field. These variation data were available with 1-min resolution, which is unusual (often only hourly mean values are derived from photographic recordings in geomagnetic observatories). Then, hourly mean values were calculated according to the INTERMAGNET rule: an hourly mean value is computed only when 54 or more 1-min values are available for the hour (Love, 2009; St. Louis et al., 2011). For details on geomagnetic observatories and data processing, we refer to Wienert (1970), Jankowski and Sucksdorff (1996), and Matzka et al. (2010). Our final processed TTB data set is available as a data publication (Soares et al., 2020) in GFZ Data Services.

The TTB H-component daily ranges (hereinafter referred to as H_A ranges) were computed from the hourly mean values by these three steps: Dst field correction as explained in section 2.4; main field removal by subtracting a linearly interpolated baseline constructed from nighttime (22 to 02 LT) averages; and finally, selection of the maximum value between 10 and 14 LT for each day.

2.2. Additional Ground-Based Data

Additional hourly mean values from the geomagnetic observatories Kourou (KOU, 5.2°N, 52.7°W) and Paramaribo (PAB, 5.8°N, 55.2°W) were used as low-latitude reference stations in the investigation of CEJ occurrence at TTB. Their data were downloaded from INTERMAGNET (www.intermagnet.org, data from 1996 to 2019) and WDC Kyoto (http://wdc.kugi.kyoto-u.ac.jp/, data from 1964 and 1965), respectively. Unlike TTB, the geomagnetic observatory Huancayo (HUA, 12.0°S, 75.3°W) remained close to the magnetic equator since its establishment in 1922 and, for this reason, its data from 1957 to 2019 (Soares et al., 2020) were used for comparison.

2.3. Satellite Data

High-precision geomagnetic data from the Challenging Minisatellite Payload (CHAMP) and Swarm satellite missions were used. CHAMP is a German satellite that operated from July 2000 to September 2010 (Reigber

et al., 2002). Swarm is a constellation of three satellites launched in November 2013 (Friis-Christensen et al., 2006, 2008).

In this work we used quiet time (Kp index ≤ 3) electric current intensity profiles for a quasi-dipole (QD) latitude range of −20° to +20° derived from both CHAMP (2000 to 2010) and Swarm (spacecraft A and B, 2013 to 2018) magnetic field data. Here we used CHAMP and Swarm current profiles with latitudinal resolutions of 0.25° and 0.5°, respectively. They were obtained after removing the core (by the CHAOS-6 model, Finlay et al., 2016), lithospheric (by the MF7 model, Maus et al., 2008), magnetospheric (by the POMME-6 model, Maus & Lühr, 2005), and Sq (by fitting a low-degree spherical harmonic field model to the higher-latitude data) magnetic fields from the original magnetic field data and subsequently inverting the residual magnetic field for electric currents at an E-region height of 110 km (Alken et al., 2013, 2015).

2.4. Geophysical Indices

The Dst index (http://wdc.kugi.kyoto-u.ac.jp/dstdir/index.html) was used to correct for the disturbance field in the H-component according to Equation 1 (Yamazaki & Maute, 2017):

$$H' = H - (Dst \cdot cos\ \lambda), \tag{1}$$

where H' is the corrected H-component, H is the original H-component, and λ is the time-dependent geomagnetic latitude of the station.

In addition to the Dst field correction, we used the catalogue of international quiet days (IQDs) and disturbed days (IDDs) that are derived from the Kp index (https://www.gfz-potsdam.de/en/kp-index/). Two methods were used to constrain the analysis to geomagnetically quiet periods. For monthly average values, we used only the 10 quietest days of each month and, if more than five of these days correspond to data gaps, the month was excluded from the analysis (IQD constraint). For higher temporal resolution data, we excluded only the five most disturbed days from each month (IDD constraint).

The Dst field correction, IQD, and IDD constraints were not applied for the CEJ analysis. Instead, magnetic disturbance effects were mitigated by limiting the analysis to quiet days as selected by a Kp index criterion (Kp ≤ 3). This allows for comparison with previous studies (e.g., Marriott et al., 1979; Rastogi, 1974; Soares et al., 2019, 2018). The sunspot number (http://www.sidc.be/silso/) was also used for the CEJ analysis in order to account for CEJ solar cycle (SC) modulation.

The monthly mean values of the observed F10.7 solar radio flux (Tapping, 2013) were used to evaluate the influence of solar activity on the range of the H-component geomagnetic daily variation and remove the related variability from the data. For the day-to-day variability analysis, daily values of F10.7 were used to normalize the H-component data.

2.5. TIEGCM Model Setup

The TIEGCM (version 2.0) was used to evaluate the effect of the change in the geomagnetic main field on the daily variation. The TIEGCM is a global three-dimensional, time-dependent model of Earth's upper atmosphere (97 to 600 km), developed at the National Center for Atmospheric Research (Qian et al., 2014; Richmond et al., 1992). The model configuration used here has a horizontal resolution of 2.5° in latitude and longitude and a vertical resolution of four grid points per scale height. The model uses the F10.7 index to calculate energetic solar radiation flux, which is a determining factor for heating in the thermosphere and ionization in the ionosphere. Solar wind data (including solar wind speed, density, and interplanetary magnetic field) are used to specify the ion convection pattern at high latitudes based on the empirical model by Weimer (2005). The model lower boundary is constrained by migrating solar diurnal and semidiurnal tides from the Global Scale Wave Model (Hagan & Forbes, 2002, 2003), which mimics tidal forcing effects on the ionosphere/thermosphere system.

We performed simulations for 1961 and 2015. These years were selected because they have similar solar flux and geomagnetic activity conditions. The yearly average of the F10.7 index was 105.4 and 118.0 sfu (solar flux unit) for 1961 and 2015, respectively. The yearly average of the Ap index was 14.4 and 12.3 nT for 1961 and 2015, respectively. Both simulations were run with identical parameters except for the geomagnetic main field which was altered according to the IGRF. The F10.7 and solar wind inputs used for these runs correspond to conditions in 2015. The final TIEGCM outputs used in this work are hourly values of
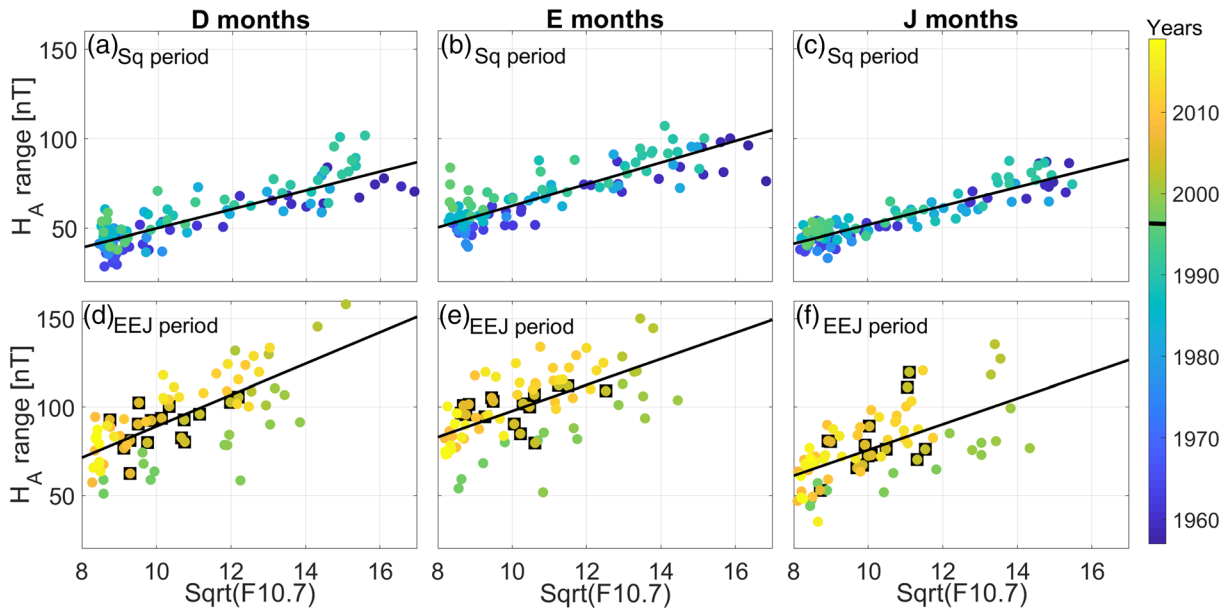
Figure 2. Monthly averages of TTB H_A range versus $\sqrt{F10.7}$ for D (Sq in panel (a) and EEJ in panel (d)), E (Sq in panel (b) and EEJ in panel (e)), and J (Sq in panel (c) and EEJ in panel (f)) months. The color code indicates the year (from 1957 to 2019). The black lines are linear fits to the data points during the Sq (1957–1996) and EEJ (1997–2019) periods. The horizontal black line in the color bar represents 1996/1997. Data that had to be converted from millimeter to nanotesla are indicated by black squares.

ground-level magnetic perturbations (i.e., variations) averaged for each month, which were calculated as described by Doumbia et al. (2007) and Richmond and Maute (2014). These hourly values can be directly compared with observatory data.

3. Results and Discussion

3.1. Solar Flux Dependence

The magnitudes of geomagnetic daily variations associated with Sq and EEJ are correlated with the level of solar activity (e.g., Briggs, 1984; Matzka et al., 2017). This is because both Sq and EEJ currents are controlled by ionospheric conductivities, which linearly vary with the electron density. Under photochemical equilibrium conditions, the electron density is proportional to the square root of the EUV flux, and hence its proxy F10.7 (Yamazaki & Kosch, 2014). Therefore, the daily H range is expected to be proportional to the square root of F10.7. Figure 2 shows the relationship between the H_A range and the square root of F10.7. Figure 2 top row shows data for a reference "Sq period" (1957 to 1996) and the bottom row for a reference "EEJ period" (1997–2019). These periods were based on the fact that, in 1996/1997, TTB was 3° away from the magnetic equator. Each column of Figure 2 stands for one of the three Lloyd seasons of the year: D (December solstice: November to February), E (equinox: March–April and September–October), and J (June solstice: May to August) months. Each circle in Figure 2 represents a monthly average (after IQD constraint) of H_A ranges and $\sqrt{F10.7}$, color-coded according to the year of observation. Circles with a black square in Figure 2 correspond to the months for which TTB data had to be converted from millimeter to nanotesla. On average, these data match well with the overall trend, confirming the validity of our data conversion technique. Regression lines were fit for the reference Sq and EEJ periods (black lines). It is noted that these regression lines depend on seasons.

It is necessary to remove the solar flux influence (Figure 2) in order to isolate the effect of secular variation on the daily H_A ranges. First, we divided TTB data in 15 subsets according to years and seasons (Table 1). Next, a linear fit (analogous to those presented in Figure 2) was computed for each data subset through an iteratively reweighted least squares algorithm (Farquharson & Oldenburg, 1998), aiming for a robust fit. The obtained slopes (s) and intercepts (i) as well as the RMS error of the fit are listed in Table 1. The RMS error is greater for the EEJ period, as expected from its higher variability observed in Figure 2.

Table 1
Slope (s, in nT/√sfu) and Intercept (i, in nT) of the Linear Fits Between H_A Range and $\sqrt{F10.7}$ for 15 Subsets Used to Normalize H_A Data

	D months			E months			J months		
Period	s	i	RMS	s	i	RMS	s	i	RMS
1957–1965	5.00	−5.91	6.11	5.88	−0.51	6.51	5.53	−5.64	4.93
1976–1986	4.26	7.33	7.47	6.06	0.49	6.53	3.87	12.04	4.92
1987–1996	5.82	−3.33	7.54	5.29	16.70	7.94	5.49	−0.73	5.30
1997–2008	9.80	−18.06	16.81	6.69	24.15	16.95	7.01	−0.02	17.64
2009–2019	10.62	−9.69	9.22	10.81	−5.54	11.06	10.66	−25.04	11.50

Note. The corresponding RMS error (in nT) of the fit to the observed data is also shown. Data from 1966 to 1975 are not included in the table due to its unavailability.

The linear fits were used to normalize the H_A data to a fixed solar flux level of 100 sfu according to

$$H_N = H_A \cdot \frac{s(p) \cdot \sqrt{100} + i(p)}{s(p) \cdot \sqrt{F10.7} + i(p)}, \tag{2}$$

where H_N is the normalized H_A range, s and i are the linear regression coefficients (slope and intercept, respectively), p stands for corresponding subsets in Table 1, and $F10.7$ is the F10.7 value for the corresponding month (or day, in the case of day-to-day variability analysis).

3.2. Transition From Sq to EEJ

Figure 3a shows the year-to-year variation of the Dst-corrected, IQD-constrained, and F10.7-normalized H_N range at TTB. The average yearly values of H_N are shown as dark blue squares and will be the metric used for discussion hereinafter. For completeness, the data used to calculate these averages are also shown as circles for each year (in light blue for those found within the standard deviation σ interval and in light gray for those found beyond σ interval). The QD latitude decreases almost linearly with time at TTB (Soares, Matzka, et al., 2018) and the upper x axis in Figure 3a indicates corresponding QD latitude values. A gradual enhancement of H_N happens from 1981 to 1999 (about 11 nT change in 18 years), and a steeper gradient is observed from 1999 to 2001 (about 25 nT change in 3 years). Around 2013, when TTB QD latitude is zero, H_N reaches twice its initial value from 1957. The large increase in the H_N range can be explained by the transition of the daily variation from the Sq type to the EEJ type. For a comparison, Figure 3b shows an analogous plot using
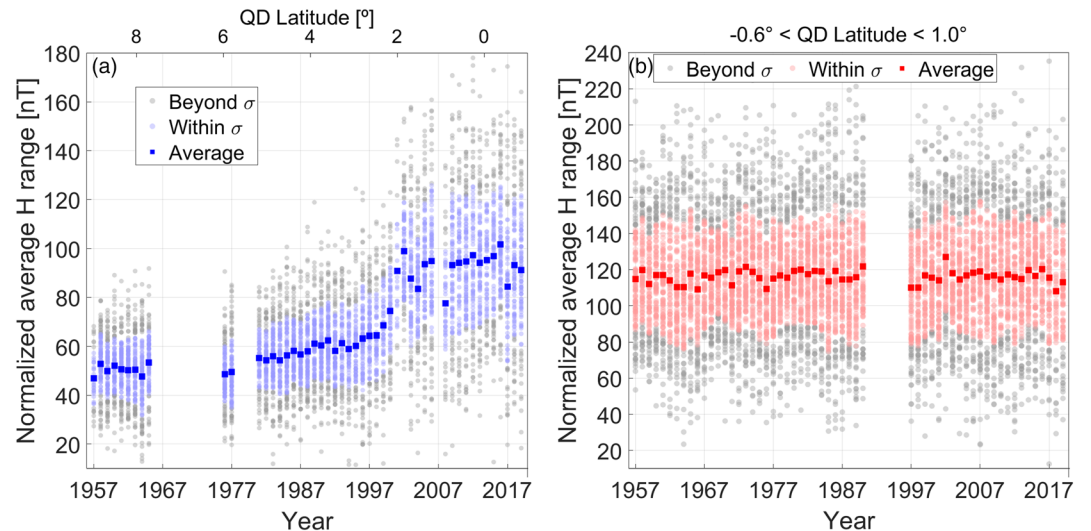

Figure 3. (a) Average yearly values of H_N range at TTB (dark blue squares). Light blue circles show data found within the standard deviation σ interval. Light gray circles show data found beyond σ interval. (b) Same as panel (a), but for HUA (red color is used instead of blue). The corresponding QD latitudes are shown in the upper abscissa.
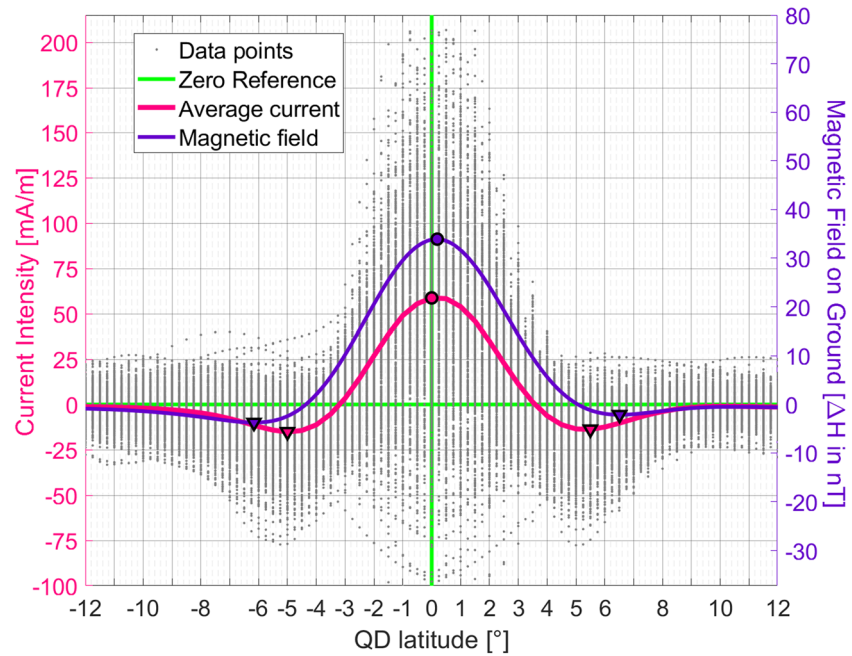
Figure 4. Quasi-dipole (QD) latitudinal profile of satellite-derived (CHAMP and Swarm) height-integrated current intensity (gray dots) and its average (magenta line) in the Brazilian sector (43.5°W to 53.5°W). Associated magnetic field at ground level is calculated by a line current model and shown by the purple line. Only quiet (Kp ≤ 3) noon-time (from 10 to 14 LT) data from 2000 to 2018 are used. The EEJ maximum and return current minima values are shown by a circle and triangles in both current and magnetic field curves.

HUA H_N range data (average yearly values shown as dark red squares). HUA H_N range values are greater than those observed for TTB but are rather constant with time at around 115 nT. This is because HUA has been always inside the EEJ region, with QD latitudes varying nonlinearly from −0.6° to 1.0°.

To further characterize the EEJ magnetic signals at TTB, we use the combined CHAMP and Swarm satellite data set. Figure 4 shows the noon-time (10 to 14 LT) current intensity data (gray dots) along a QD latitudinal profile over the Brazilian sector (between 43.5°W and 53.5°W, centered at TTB longitude). Only quiet (Kp ≤ 3) data are used. The average height integrated current intensity was calculated by a moving average of 0.5° in length and is shown by the magenta line. Since the large-scale Sq field is removed from the data in preprocessing, the peaks in the magenta line represent the EEJ and its return currents. We also calculated the magnetic field on the ground from this current intensity profile by using discrete line currents at 108 km height and mirror currents at a depth of 200 km. This approach is based on Lühr et al. (2004) and Onwumechili and Ezema (1992) and yields the sum of the EEJ external and induced magnetic field components, which is shown by the purple line in Figure 4. The zero references for both *x* and *y* axes are shown by green lines.

The circles in Figure 4 indicate the EEJ peak, which occurs at 0.0° for the current intensity and 0.2° for the magnetic field. Given the usage of a moving average of 0.5°, there is an uncertainty of ±0.25° in the QD latitude of the current intensity values. A correspondent uncertainty of ±0.24° was estimated for the magnetic field profile on ground by taking the current intensity QD latitude error margin into account during its calculation. This is in reasonable agreement with the results of Lühr et al. (2004), who used CHAMP data from 2000 to 2003 and indicated that the EEJ peak occurs between −0.2° and 0.2° (within the ±1 sigma uncertainty interval) for the Brazilian sector. Rastogi et al. (2008) estimated the EEJ center position by using data from 1994 recorded by three magnetometer stations in Central Brazil (found within ±2° of dip latitude). They determined the EEJ center by identifying where the vertical component daily range was zero after interpolating its values over the three stations. For noon-time, they found that the EEJ peak occurs between approximately −0.4° and −0.8° (with an error of ±0.25°), which slightly deviates from the magnetic field result presented here (0.2 ± 0.25° magnetic latitude). The discrepancy could be due to the fact that Rastogi et al. (2008) did not separate large-scale (Sq) and local-scale (EEJ) fields.
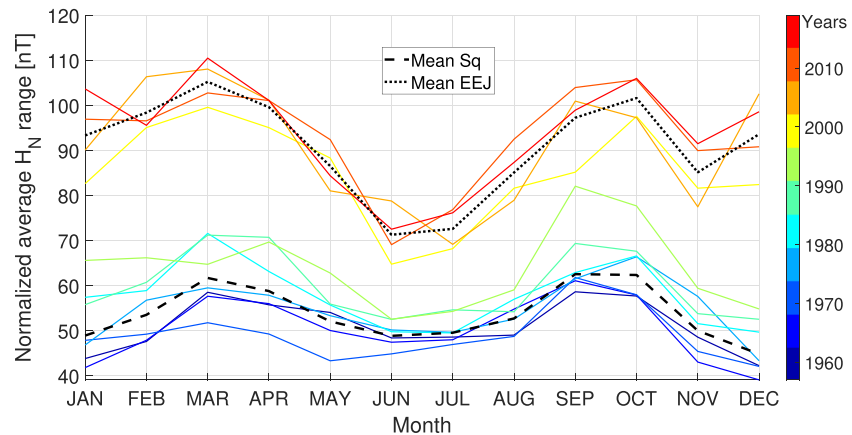
Figure 5. Seasonal variation of the normalized H_N range at TTB. Each solid line represents a 5-year period (color-coded according to the corresponding epoch). The Sq and EEJ averages are represented by dashed and dotted black lines, respectively.

From southern to northern QD latitudes, the satellite-based current intensity profile shows that the normal EEJ region (magenta line positive values in Figure 4) extends from −3.2° to 3.5° QD latitude. In the ground magnetic field profile, this region extends from −4.3° to 5.0°. Therefore, both current intensity and magnetic field indicate some south-north asymmetry in the EEJ. Still inside the normal EEJ region, we could find the QD latitudes of maximum EEJ rate of enhancement by applying the first derivative (not shown here) to the current intensity and magnetic field profiles. These are 2.0° for the current intensity and 2.7° for the magnetic field. This agrees with the steep H_N range increase at TTB around the year 2000, which occurred in a coincident QD latitude (Figure 3a).

The QD latitude of 5.0° corresponds to the beginning of the EEJ enhancement at TTB, in the 1980 decade (Figure 3a). This indicates that the EEJ contributed to the observed H_N gradual enhancement at TTB during the 1980s and 1990s. However, the Sq field also played a role in this H_N gradual enhancement, either by its temporal or spatial variations. Using south hemisphere magnetic ground data from 1964 to 2007, Torta et al. (2010) showed that no systematic drift occurred in the Sq focus latitudinal position. Thus, with a Sq system that largely maintained its shape throughout the years, the main Sq-related variation is its spatial variation in H, which is smaller near the Sq focus and larger at lower latitudes (Takeda, 1999). Therefore, spatial changes of both EEJ and Sq contributed to the H_N variation observed at TTB during 1980s and 1990s.

Asymmetries between the southern and northern return currents are observed in Figure 4. Their peaks (indicated by triangles) are located at −5° and 5.5° for current intensity and −6.2° and 6.5° for magnetic field. The return currents also differ in their peak amplitudes, from south to north: −15.1 to −13.7 mA/m for current intensity and −3.7 to −2.1 nT for magnetic field. Zhou, Lühr, & Alken (2018) also indicated that the northern return current is weaker when compared to its southern correspondent in the longitude sector that TTB is found. It is difficult to analyze return current effects with the available TTB data set because it is a weak signal (2.1 nT) that peaks at 6.5° QD latitude, during the major data gap in TTB (Figure 1d).

3.3. Seasonal Dependence

Figure 5 shows the seasonal variation of the Dst-corrected, IQD-constrained, and F10.7-normalized H_N range. Each solid line corresponds to a 5-year average within the Sq and EEJ periods (i.e., 1957 to 1961, 1962 to 1966, …, 2010 to 2014, 2015 to 2019). These lines are color-coded according to the period that they represent. The averaged patterns for the Sq (1957 to 1994) and EEJ (2000 to 2019) periods are shown as the dashed and dotted black lines, respectively, excluding the 1995 to 1999 transition data. A characteristic seasonal pattern is observed: the Sq period shows equinoctial maxima with solstitial minima (peak-to-peak amplitude of about 18 nT), while the EEJ period shows equinoctial maxima with a more prominent minimum during June–July (peak-to-peak amplitude of about 34 nT).

The semiannual variation in the H_N range at low and equatorial latitudes is known from previous studies (Campbell, 1982; Chapman & Rao, 1965; Stening, 1995). Yamazaki et al. (2014b) numerically showed that
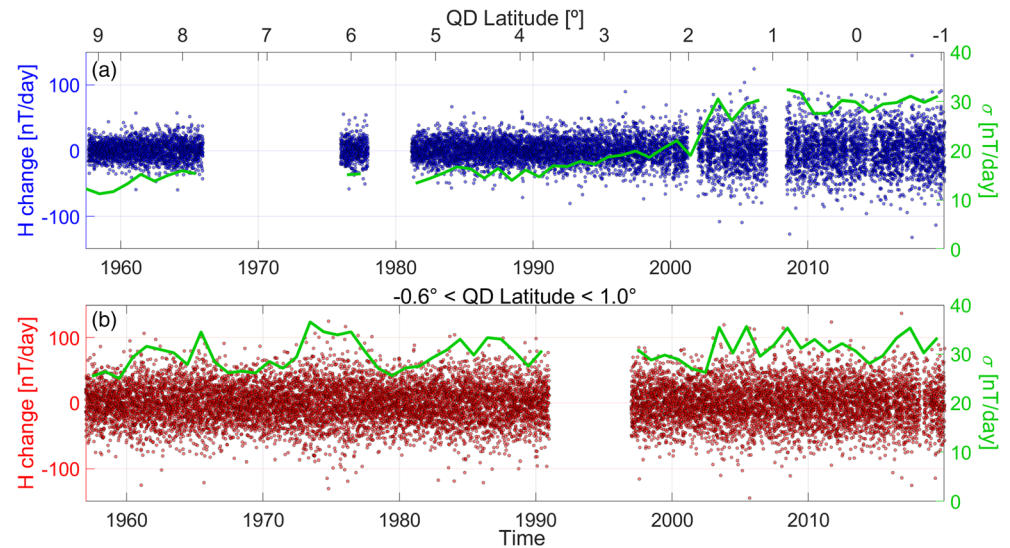
Figure 6. (a) Day-to-day variability at TTB, from 1957 to 2019 given by the difference in H_N range between consecutive days (in nT/day, blue dots). (b) Same as panel (a), but for HUA (red dots). Annual values of day-to-day variability standard deviation (σ) are shown by the green line in both panels. TTB and HUA QD latitudes are shown on the upper abscissa.

neutral wind variability due to tidal waves from the lower atmosphere is the primary driver of the semiannual variation of the EEJ. Tidal waves from the lower atmosphere also play a dominant role in the semiannual variation of Sq as shown in Yamazaki and Maute (2017). The observed differences between Sq and EEJ can arise from their different generation mechanisms: the EEJ currents are primarily electric-field-driven, while low-latitude Sq currents are partly electric-field-driven and partly local-wind-driven (Richmond & Roble, 1987).

Although the absolute values of seasonal variation amplitude increased by a factor of 2 from the Sq to the EEJ period, their relative contribution to the average daily variation stayed the same. Both Sq and EEJ average seasonal variation amplitudes (18 and 34 nT) correspond to about 35–40% of the average H_N range (50 and 95 nT, from Figure 3a). The main features of Sq and EEJ seasonal variations in TTB are in agreement with those obtained by Yamazaki et al. (2010) for the 120° to 130° longitude sector. The average EEJ seasonal variation in TTB also agrees with results obtained from ground-based magnetic data for other longitudes (Rastogi et al., 1994; Shume et al., 2010; Tarpley, 1973) and with satellite measurements over Brazil (Alken & Maus, 2007; Soares 2018).

3.4. Day-to-Day Variability

The quiet time geomagnetic daily variation is subject to day-to-day changes in its amplitude and shape. A large part of the day-to-day variability is not yet fully understood (Yamazaki & Maute, 2017). Simultaneous measurements at equatorial and low-latitude stations indicate that the H range day-to-day variability differs significantly between the Sq and EEJ (Hamid et al., 2014; Mann & Schlapp, 1988; Yamazaki et al., 2014a). With the long-term data from TTB, it is possible to investigate how the day-to-day variability gradually changed from the Sq to the EEJ period. Figure 6a shows the observed H_N range differences between consecutive days for TTB (in nT/day, blue dots) as a measure of day-to-day variability, after Dst correction, IDD-constraint, and F10.7 normalization. Annual values of day-to-day variability standard deviation are shown by the green line.

The day-to-day variability shown in Figure 6a indicates periods of lower variability from 1957 to the early 1990s (Sq type), gradual variability enhancement during the 1990s, and higher variability from 2000 to 2019 (EEJ type). This behavior can be easily identified by the annual values of day-to-day variability standard deviation. Such a long-term change is not observed at HUA (Figure 6b), where the change in the location of the magnetic equator is small (Figures 1b and 1c).
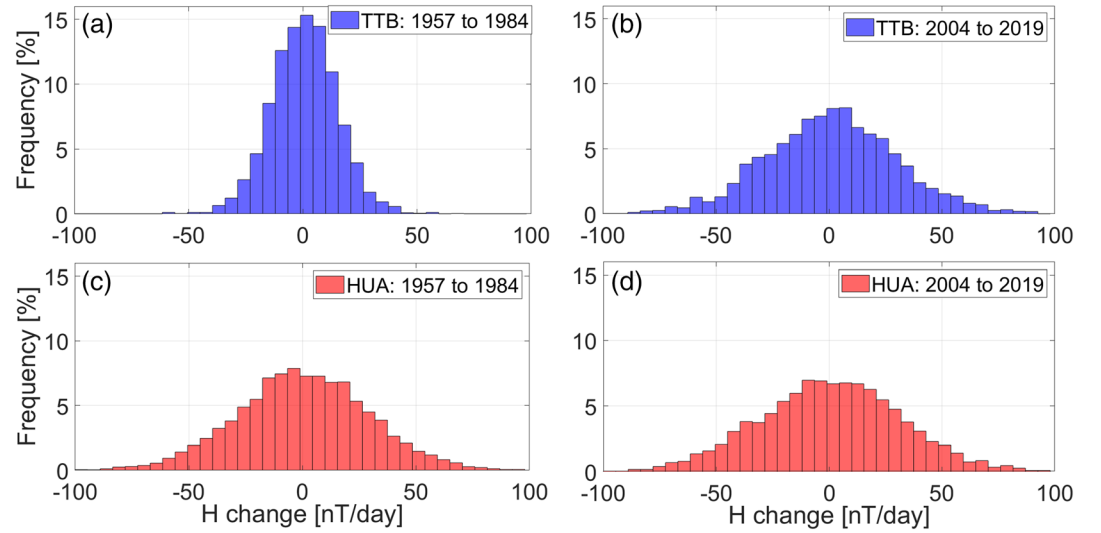
Figure 7. (a) Histogram of day-to-day variability values observed at TTB from 1957 to 1984 (Sq period). (b) Same of panel (a), but from 2004 to 2019 (EEJ period). (c) Same of panel (a), but for HUA. (d) Same of panel (b), but for HUA.

Figure 7 shows histograms of day-to-day variability values for TTB (panels a and b) and HUA (panels c and d) during the periods of 1957 to 1984 and 2004 to 2019. These periods were chosen in a manner that they correspond to Sq and EEJ periods at TTB, respectively, and to a similar amount of data, what is convenient for a statistical comparison. Table 2 summarizes some statistical measures of each distribution shown in Figure 7: sample mean ($\bar{x}$), sample standard deviation (s), and sample size (n).

Visually, the histogram distributions for HUA and for the EEJ period in TTB are similar (Figures 7b–7d), while the Sq period in TTB (Figure 7a) differs significantly. In addition, Table 2 shows similar sample means for all distributions, but a distinctly different standard deviation of 14.4 nT for TTB (1957 to 1984) as compared to 29.57, 29.58, and 31.92 nT for the other cases. This implies an enhancement of the day-to-day variability by a factor of 2 at TTB for the EEJ period, which does not occur at HUA.

This comparison suggests that the change in the distance to the magnetic equator is the likely cause for the increased day-to-day variability observed at TTB, while long-term changes in the variability of magnetospheric and atmospheric forcing, which would affect both TTB and HUA data similarly, play only minor roles. It is interesting to note that the magnitude of the day-to-day variability relative to the average H_N range (50 and 95 nT, from Figure 3a) is approximately 30% for both Sq and EEJ periods.

As known from previous studies, upward propagating tides and other large-scale waves from the lower atmosphere cause the day-to-day variation of the ionospheric wind dynamo, which therefore leads to the Sq and EEJ day-to-day variability (Fang et al., 2013; Miyahara & Ooishi, 1997; Yamazaki et al., 2014a). Zonal and meridional wind components of those waves produce currents $\Delta \mathbf{J_w} = \sigma (\Delta \mathbf{U} \times \mathbf{B})$, where $\Delta \mathbf{J_w}$ and $\Delta \mathbf{U}$ are perturbations in the current density and winds, respectively; σ is the ionospheric conductivity tensor; and $\mathbf{B}$ is the ambient magnetic field. Subsequently, electric field perturbations $\Delta \mathbf{E}$ arise in such a manner that total perturbation currents $\Delta \mathbf{J_t}$ satisfy the divergence-free condition. That is, $\nabla \cdot \Delta \mathbf{J_t} = \nabla \cdot [\sigma (\Delta \mathbf{E} + \Delta \mathbf{U} \times \mathbf{B})] = 0$. For the EEJ, σ is replaced by the Cowling conductivity σ_C, as the presence of the vertical electric field over the magnetic equator leads to an increase in the effective zonal conductivity (Richmond & Roble, 1987). Therefore, for both Sq and EEJ, the ratio of the perturbation currents to the background currents can be expressed in the form $(\Delta \mathbf{E} + \Delta \mathbf{U} \times \mathbf{B})/(\mathbf{E_0} + \mathbf{U_0} \times \mathbf{B})$, where $\mathbf{E_0}$ and $\mathbf{U_0}$ are the components of the electric field and winds that do not vary from day to day. Our results suggest that the magnitude of the day-to-day variability is significantly greater for the EEJ than Sq, which can be understood as $\sigma_C > \sigma$. Meanwhile, the relative magnitude of the day-to-day variation to the

Table 2

Summary of Statistical Measures of Each Distribution of TTB and HUA Day-to-Day Variability, Including Sample Mean ($\bar{x}$), Sample Standard Deviation (s), and Sample Size (n)

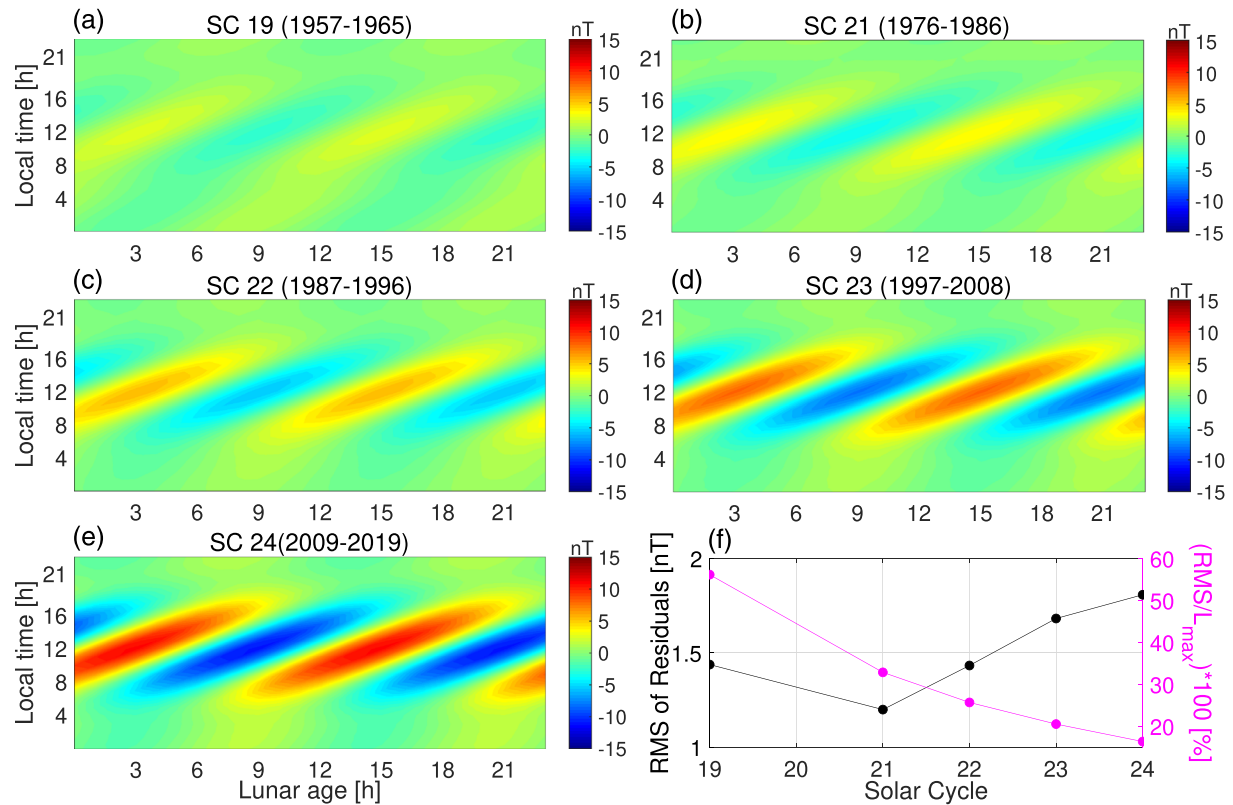| Sample	$\bar{x}$ (nT)	S (nT)	n
TTB (1957 to 1984)	0.73	14.44	3,527
TTB (2004 to 2019)	0.89	29.57	3,411
HUA (1957 to 1984)	0.38	29.58	7,321
HUA (2004 to 2019)	0.59	31.92	4,021

Figure 8. Predicted average amplitude of the lunar variation L (in nT) in TTB H-component, as a function of local time and lunar age, during solar cycles (SC) 19 (a), 21 (b), 22 (d), 23 (d), and 24 (e). The RMS values of the residuals (error in nT, black circles) and their relation to the maximum L variation amplitudes (in %, magenta circles) are shown in (f).

mean value is comparable for the EEJ and Sq because the relative magnitude is not sensitive to the ionospheric conductivity as shown above.

3.5. Lunar Variation

In order to isolate the lunar variation (L), the TTB H-component hourly data was first Dst corrected and IDD-constrained. Then, the average solar variation was evaluated at each local time of each day as the average over ±14 days at the same local time and then removed from the data, following the approach of Yamazaki and Maute (2017). The resulting hourly data were grouped according to SC periods identical to those in Table 1. The L amplitudes were determined by fitting the following equation independently to data from each SC period.

$$L(t,\nu) = \sum_{n=1}^{4} A_n \cdot \sqrt{F10.7} \cdot sin\left(n\frac{2\pi}{24}t - 2\frac{2\pi}{24}\nu + \varepsilon_n \right). \qquad (3)$$

Equation 3 is based on Chapman's phase law (Chapman, 1919), where t and ν are the local time and lunar age (phase) in hours, and A_n and ε_n are amplitude and phase parameters determined through ordinary least squares inversion (Çelik et al., 2012; Malin, 1970; Malin & Chapman, 1970). The F10.7 term included in Equation 3 acts as a weighting factor and a solar flux of 100 sfu is used for normalization when calculating predicted L variations. All fits are based on more than 2,200 days for each SC.

Figures 8a–8e show the predicted L variations at TTB as a function of local time and lunar age for each SC period. Note that SC 20 is not shown due to lack of data. SCs 19 and 21 show a consistently smooth semimonthly L variation reaching amplitudes between 2.5 and 4 nT (Figures 8a and 8b). From SC 22 to SC 24, the L amplitude gradually increases (Figures 8c–8e). The SC 22, already under the influence of the EEJ, presents an amplitude of 5.5 nT. SC 23 corresponds to the period of highest H range rate of change due to the increasing EEJ at TTB, and the L amplitude reaches 8 nT. In SC 24, epoch of minimum magnetic equator
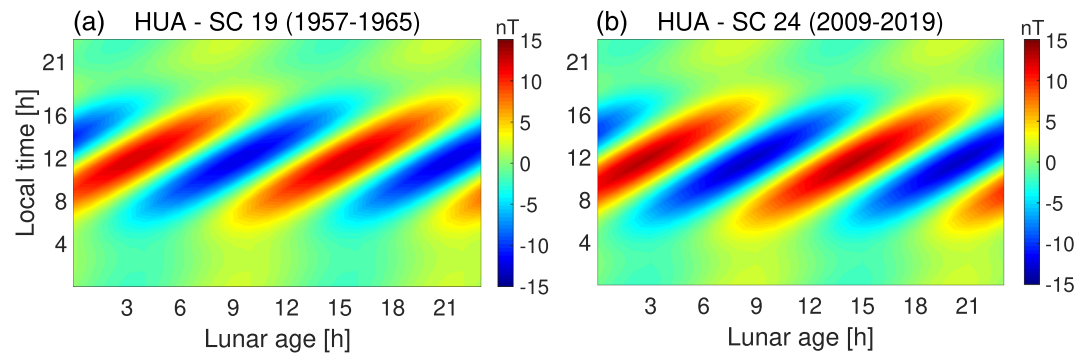
Figure 9. Predicted average amplitude of the lunar variation L (in nT) in HUA H-component, as a function of local time and lunar age, during solar cycles (SC) 19 (a) and 24 (b).

distance to TTB, the L amplitude is largest with 11 nT. Interestingly, the amplitude of L divided by the average H_N increased from ~5% (2.5 nT divided by 50 nT for SC 19) to ~12% (11 nT divided by 95 nT for SC 24) at TTB. This indicates that, for the Brazilian sector, the EEJ is more sensitive to lunar tides than Sq is.

RMS values of the residuals (differences between predicted and observed L amplitudes, black circles in Figure 8f) are between 1 and 2 nT, which corresponds to less than 35% of the maximum L variation amplitudes (magenta circles in Figure 8f), except for SC 19 with 56% due to its weak L signal. As expected, the RMS increases with the increasing L amplitude due to larger EEJ signal, but its relative importance (i.e., associated error) diminishes.

The amplitude of the L variation at TTB was also determined by Malin (1973), who used data from 1957.5 to 1960.5 (a total of 706 days, Sq period in TTB). An amplitude of about 3.2 nT was obtained, which agrees with the result presented here for SC 19. For the same epoch, Malin (1973) computed L variations of about 16.2 nT at HUA, over the equator. There is no solar flux normalization in Malin's analysis.

For a comparison, we performed the same analysis with HUA data from SCs 19 and 24 (Figures 9a and 9b). Unlike at TTB, nearly identical results were obtained for both SCs with maximum amplitudes of 12.2 and 13.3 nT, respectively. These results are comparable to those of Malin (1973) and Yamazaki and Maute (2017). Thus, the L amplitudes at HUA (Figure 9) and TTB (mainly during SC 24, Figure 8e) are similar, as both are under EEJ conditions. The relative amplitude of L at HUA was rather constant over time: ~11% (12.2 nT of 115 nT) and ~12% (13.3 nT of 115 nT) for SCs 19 and 24, respectively.

3.6. Counter-Electrojet Occurrence

Upon entering the EEJ region, the H-component magnetic daily variation at TTB started to show, occasionally, depressions of the field below the nighttime base line, which is likely due to CEJ events. To investigate the CEJ occurrence at TTB, we used the same method as Soares et al. (2019), based on the difference between the H hourly values from a pair of stations (one in the equatorial region and the other at low-latitude). We used the TTB-KOU pair and investigated CEJ occurrences since the year 1996, when the KOU time series started. For the CEJ analysis, we do not correct the TTB data for the Dst field, as it is largely removed when the difference is taken for H observed at two closely located stations. To allow direct comparison with earlier studies, we do not normalize the data with F10.7. Only geomagnetically quiet days, selected based on the Kp index, were used.

The annual rates of morning (MCEJ, 6 to 10 LT) and afternoon (ACEJ, 14 to 18 LT) counter electrojet events at TTB are shown in Figure 10a together with the annual values of sunspot number given by the gray area. The corresponding QD latitude of TTB is shown on the upper abscissa. The results from SC 24 (2009–2019) indicate a predominance of MCEJ and an anticorrelation of ACEJ with the SC, which is consistent with previous results for the years 2008 to 2018 (Soares et al., 2018, 2019). For SC 23 (1996–2008), we find very low MCEJ rates of around 15% from 1996 until 2001. A jump in MCEJ rates occurs from 2001 to 2002, which is the period of highest increase of EEJ signal, as indicated in Figures 3 and 4. During the SC 24, an average rate of 50% was observed for MCEJ. On the other hand, the ACEJ rates show very similar values and behavior during both SCs 23 and 24.
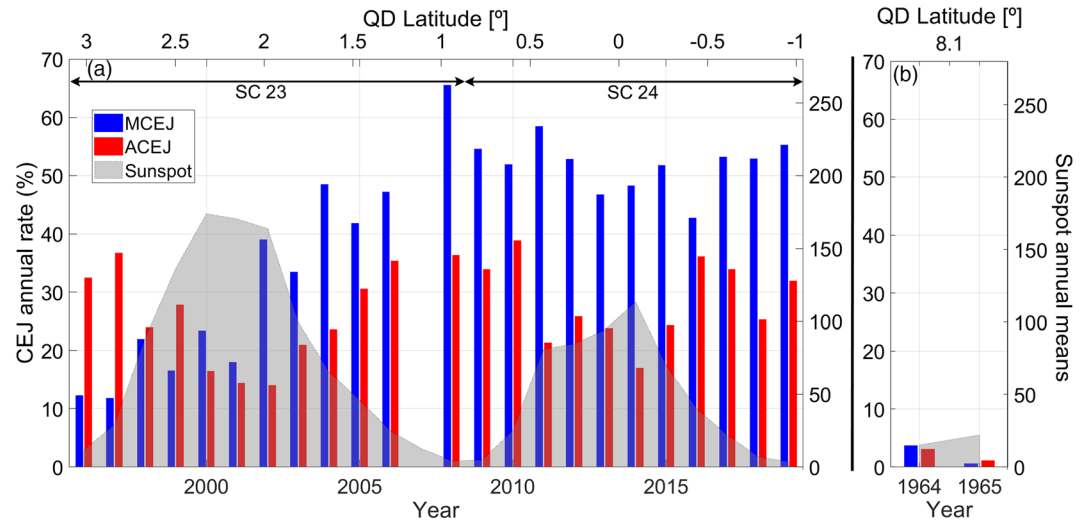
Figure 10. (a) Annual occurrence rates of morning (MCEJ, blue bars) and afternoon (ACEJ, red bars) counter electrojet events at TTB derived from the TTB-KOU pair during 1996–2019. (b) Same as panel (a) but for the TTB-PAB pair during 1964–1965. Annual means of sunspot number are shown as a gray area in both panels. TTB QD latitude is shown in the upper abscissa. Solar cycles 23 and 24 are indicated by black arrows.

For a comparison, Figure 10b shows the same analysis using the pair TTB-PAB for the years 1964 and 1965. In this case, both TTB (1965 QD latitude: 8.1°) and PAB (1965 QD latitude: 17.1°) were located outside the EEJ influence. As expected, very low rates are observed in both cases (less than 5%). This indicates that the rates observed from 1996 to 2001 at TTB (between 10% and 40%) actually refer to CEJ events, which in addition, preserve the SC modulation of ACEJs. Another MCEJ and ACEJ feature that is preserved from SC 23 to 24 is their seasonal variation (not shown here but similar to the results presented by Soares et al. 2018).

With these observations, one question arises: why does the MCEJ behave differently during 1996–2001 and 2002–2019 while the ACEJ does not? To answer this question, we analyzed the combined CHAMP and Swarm satellite current intensity data. Figure 11 shows the occurrence rate of westward currents for both morning (blue) and afternoon (red) periods, as a function of QD latitude for the Brazilian sector (between 43.5°W and 53.5°W, centered at TTB longitude). Each rate value was calculated by a moving window of 1° of QD latitude, which was moved in steps of 0.5°. Thus, each rate represents the percentage of negative current intensity values in relation to the total data points found in the QD latitude window. Two different thresholds were used to detect negative current densities: −5 (shown in Figure 11) and −10 mA/m (similar results, not shown here). We will focus on the area between the two vertical black dashed lines in Figure 11, which represents the EEJ region (±3.5° QD latitude, according to the latitudinal profile shown in Figure 4), where westward current rates indicate CEJ occurrence rates. The peaks in the westward current rates outside the EEJ region (near 5°) indicate the return currents flow, which are not discussed in this section.
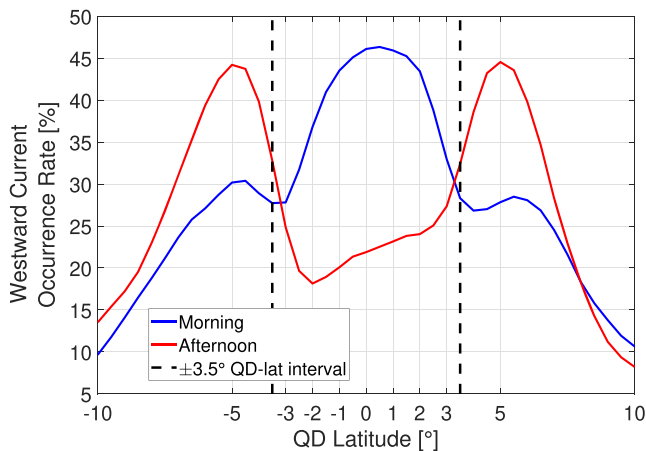

Figure 11. QD latitudinal profile (−10° to +10°) of westward current occurrence rate at the Brazilian sector, derived from CHAMP and Swarm satellite data, considering only current intensity values below −5 mA/m. Morning (6 to 10 LT) and afternoon (14 to 18 LT) occurrence rates are shown as blue and red lines, respectively. The ±3.5° QD latitude interval (EEJ region) is shown between the two vertical black dashed lines.

In the EEJ region indicated in Figure 11, MCEJ rates have a prominent central peak at 0.5° QD latitude (EEJ central axis) and greatly exceed ACEJ rates. Indeed, the latitudinal variation of MCEJ and ACEJ rates shown in Figure 11 are quite different. This latitudinal dependence can explain the abrupt change in MCEJ rates at TTB from the years 1996 to 2001 (QD latitudes +3.1° to +2.2°) to the years 2002 to 2019 (QD latitudes +2.1° to −1.0°), and the apparent continuity of ACEJ rates at TTB, being modulated by the solar activity.
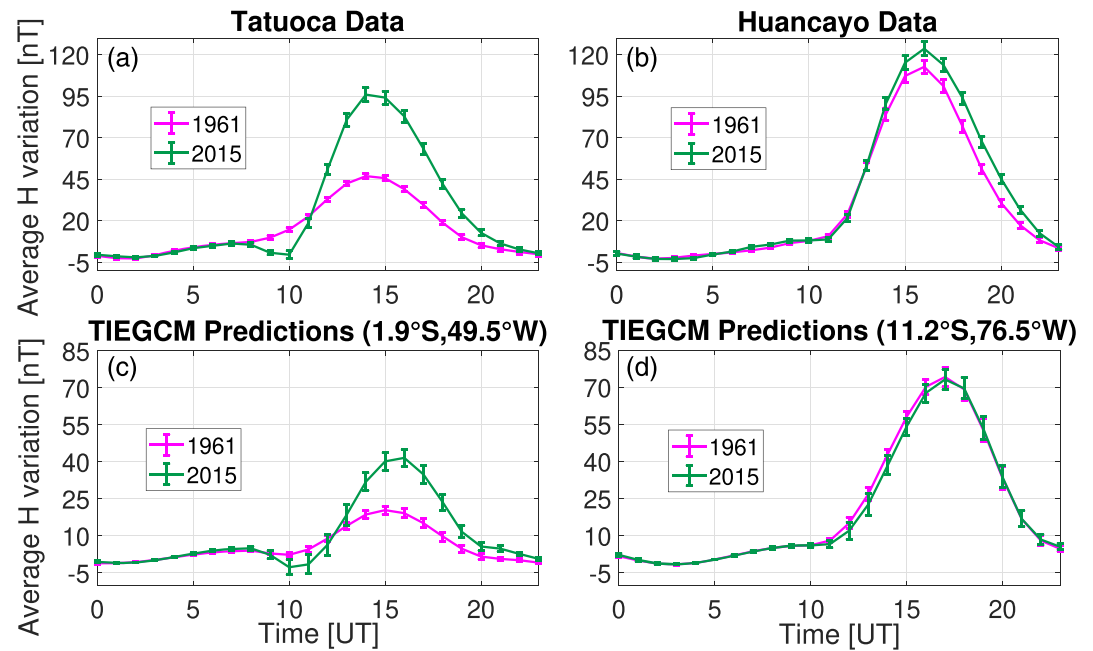
Figure 12. (a) Yearly mean geomagnetic H daily variation observed at TTB in 1961 (green line) and 2015 (magenta line). (b) Same as panel (a), but for HUA. (c) Yearly mean ground magnetic perturbations of the H-component, derived from the TIEGCM for the region of Tatuoca using the geomagnetic main field of 1961 (green line) and 2015 (magenta line). (d) Same as panel (c), but for the region of Huancayo. Error bars represent the 95% confidence interval.

The results suggest that there is a significant latitudinal variation in the CEJ occurrence rate within $\pm 3°$ magnetic latitudes, which has not been previously reported. It means that the latitudinal variation of the CEJ occurrence rates needs to be taken into account when comparing MCEJ and ACEJ rates obtained from ground stations at different epochs or longitude sectors. Thus, we highlight the importance of using equatorial stations as close to the EEJ center as possible to keep tracking the EEJ and associated CEJ events with enough precision.

3.7. TIEGCM Simulation

The average H-component geomagnetic daily variations at TTB and HUA, for 1961 and 2015, are shown in Figures 12a and 12b, respectively. In this analysis, we corrected the H-component data for the Dst field, as the TIEGCM simulation does not include the magnetospheric ring current contribution. For TTB, two distinct patterns of daily variation can be seen in 1961 (solid line) and 2015 (dashed line), as similarly shown in Figure 1a. On the other hand, the daily variations at HUA are nearly identical in 1961 and 2015. The indicated error bars represent the 95% confidence intervals and were calculated by the bootstrap technique (Efron, 1981).

The ground magnetic perturbations on the H-component obtained from the TIEGCM model are shown in Figures 12c and 12d. Due to the model resolution, we used the geographical coordinates that are nearest to TTB and HUA, which are 1.9°S/49.5°W and 11.2°S/76.5°W, respectively (interpolating the model results for TTB and HUA coordinates yields equivalent values). It is known that the model underestimates the ionospheric E-region conductivities and, hence, the amplitudes of the ground magnetic perturbations (Doumbia et al., 2007). This explains, at least in part, the different absolute values obtained for the observations and model predictions. Thus, in what follows, a comparison between data and model is made only in a relative sense.

For TTB noon-time, considering the error margins, data, and model indicate an increase from 1961 to 2015 within the intervals of 89% to 120% and 73% to 139%, respectively. For HUA noon-time, data indicate an increase from 2% to 18%, while the model indicates a result between a decrease of 13% until an increase of 10%. Therefore, considering the error margin, data and model represent the same relative change in the

noon-time daily variation. Data and model also agree that large changes occurred at TTB and small changes occurred at HUA from 1961 to 2015. This means that the differences in the geomagnetic main field due to secular variation can explain the change in the H-component daily variation observed at TTB, since the only difference between the two simulations is the geomagnetic main field, based on the IGRF.

Previous studies also performed numerical simulations to investigate long-term changes in geomagnetic daily variations. Cnossen and Richmond (2013) used the Coupled Magnetosphere-Ionosphere-Thermosphere (CMIT) model to simulate the effects of the geomagnetic main field variations over a century and found that the secular variation is the dominant cause of slowly varying changes in the ionosphere over the Atlantic region. They predicted that, in this region, strong changes would occur in the amplitude of the Sq variation, which we confirmed using TTB long-term observations. By using CMIT simulations and ground-based geomagnetic data from 1960–2000, de Haro Barbas et al. (2013) concluded that the secular variation is the main cause of the long-term changes in the Sq amplitude. They suggested a future study involving stations that experienced a large shift in their position with respect to the magnetic equator, which is accomplished in this work with TTB data and TIEGCM simulations.

Besides the field geometry, the field intensity also plays a role on the geomagnetic daily variation, as it controls the ionospheric conductivities (Cnossen, 2017; Takeda, 1996). Studies have found small increases in Sq and EEJ strengths during the last decades, which can be attributed, at least in part, to the overall reduction of the main field intensity (Elias et al., 2010; Matzka et al., 2017). It is beyond the scope of this work to separate the effect of the field intensity and the effect of the field geometry on the daily variation recorded at TTB.

4. Summary and Conclusions

A new ground-based geomagnetic data set from Tatuoca observatory (TTB, 1.2°S, 48.5°W) in Brazil has been recovered, processed, and analyzed. It provides information on the daily variations at both low and equatorial latitudes. TTB geomagnetic observatory has been operating for more than 60 years in an area where the magnetic equator moves at its fastest rate, with an average of 19 km/year since 1957.

This unique condition allows us to examine long-term changes due to geomagnetic secular variation on the daily variation of the measured H-component, using data from 1957 until 2019. This period includes the transition of the daily variation from the low-latitude Sq type to the equatorial EEJ type. In particular, long-term trends in the H range day-to-day variability were investigated for the first time in the Brazilian sector. In addition, we separated the effect of other important variables that influence the daily variation, such as solar activity, seasonal variation, and lunar variation. To facilitate the interpretation of our results, we use satellite derived current intensity profiles and two TIEGCM simulations with different configurations of the geomagnetic main field. The main findings of this work include the following:

1. A comparison of ground observations at TTB and magnetic field at ground level calculated from satellite-derived current profiles provided the latitudinal extent of the EEJ in the Brazilian sector. We found that the EEJ region extends from −4.3° to 5.0° QD latitude and peaks at 0.2° QD latitude. The northern EEJ return current as seen in the ground magnetic field peaks at 6.5°, while the southern return current peaks at −6.2°. The northern return current magnetic field amplitude is 1.8 times weaker than the southern.
2. The daily H range at TTB has increased over time (1957 to 2019) by a factor of 2, reflecting the transition of the daily variation from the Sq type to the EEJ type.
3. The relation between the H daily variation range and the square root of the solar flux has changed over time, and different linear relations were obtained for the Sq and EEJ periods.
4. The H range seasonal variation at TTB shows larger amplitudes during the EEJ period. However, the Sq and EEJ seasonal variation amplitudes relative to the average daily range remained at a similar level (35–40%).
5. The day-to-day variability at TTB during the EEJ period was found to be higher than during the Sq period by a factor of 2. The magnitudes of the day-to-day variability relative to the average daily range remained at 30% during both Sq and EEJ periods.
6. The amplitude of the lunar variation L in TTB H-component increased from SC 19 to 24. The L amplitude relative to the average daily range increased from 5% to 12%. This indicates that the EEJ in the Brazilian sector is more sensitive to lunar tides than Sq is.

7. At TTB, the MCEJ occurrence rate changed from 15% to 50% within the QD latitude interval from +3° to 0°, whereas the ACEJ remained at similar levels and maintained the well-known SC modulation. This result agrees with the latitudinal gradients of MCEJ and ACEJ occurrence rates in the Brazilian sector, as revealed by satellite data. It is suggested that the latitudinal dependence of the CEJ occurrence rates should be taken into account in CEJ studies, even for QD latitudes smaller than 3°.

8. Two TIEGCM simulations were performed: one with the geomagnetic main field of 1961 and the other with the main field of 2015. The model was able to reproduce the different patterns of the geomagnetic daily variations observed at TTB in 1961 and 2015. The results indicate that the geomagnetic main field plays the dominant role in causing the long-term changes in the daily variation observed at TTB.

Data Availability Statement

TTB and HUA data used in this paper are available at GFZ Data Services (http://dataservices.gfz-potsdam.de/portal/). The CHAMP satellite was operated by the German Aerospace Center (DLR) and GFZ German Research Centre for Geosciences and its data are accessible online (http://isdc.gfz-potsdam.de/). The Swarm satellite mission is operated by the European Space Agency (ESA) and its data are available online (http://www.earth.esa.int/swarm). Natural Resources Canada provides F10.7 solar flux data online (http://www.spaceweather.ca/solarflux/sx-en.php). SILSO data/image, Royal Observatory of Belgium, Brussels, provides the sunspot number data.

References

Alken, P., & Maus, S. (2007). Spatio-temporal characterization of the equatorial electrojet from CHAMP, Ørsted, and SAC-C satellite magnetic measurements. *Journal of Geophysical Research*, *112*, A09305. https://doi.org/10.1029/2007JA012524

Alken, P., Maus, S., Chulliat, A., Vigneron, P., Sirol, O., & Hulot, G. (2015). Swarm equatorial electric field chain: First results. *Geophysical Research Letters*, *42*, 673–680. https://doi.org/10.1002/2014GL062658

Alken, P., Maus, S., Vigneron, P., Sirol, O., & Hulot, G. (2013). Swarm SCARF equatorial electric field inversion chain. *Earth, Planets and Space*, *65*(11), 1309–1317. https://doi.org/10.5047/eps.2013.09.008

Bolzan, M. J. A., Denardini, C. M., & Tardelli, A. (2018). Comparison of H component geomagnetic field time series obtained at different sites over South America. *Annales Geophysicae*, *36*(3), 937–943. https://doi.org/10.5194/angeo-36-937-2018

Briggs, B. H. (1984). The variability of ionospheric dynamo currents. *Journal of Atmospheric and Terrestrial Physics*, *46*(5), 419–429. https://doi.org/10.1016/0021-9169(84)90086-2

Campbell, W. H. (1982). Annual and semiannual changes of the quiet daily variations (Sq) in the geomagnetic field at North American locations. *Journal of Geophysical Research*, *87*(A2), 785–796. https://doi.org/10.1029/JA087iA02p00785

Çelik, C., Tunçer, M. K., Tolak-Çiftçi, E., Zobu, M., Oshiman, N., & Tank, S. B. (2012). Solar and lunar geomagnetic variations in the northwestern part of Turkey. *Geophysical Journal International*, Volume *189*,(Issue 1), 391–399. https://doi.org/10.1111/j.1365-246X.2012.05382.x

Chapman, S. (1919). The solar and lunar diurnal variations of terrestrial magnetism. *Philosophical Transactions of the Royal Society A*, *218*, 118 , 561–569. https://doi.org/10.1098/rsta.1919.0001

Chapman, S., & Rao, K. R. (1965). The H and Z variations along and near the equatorial electrojet in India, Africa and the Pacific. *Journal of Atmospheric and Terrestrial Physics*, *27*(4), 559–581. https://doi.org/10.1016/0021-9169(65)90020-6

Cnossen, I. (2017). The impact of century-scale changes in the core magnetic field on external magnetic field contributions. *Space Science Reviews*, *206*, 259. https://doi.org/10.1007/s11214-016-0276-x

Cnossen, I., & Richmond, A. D. (2013). Changes in the Earth's magnetic field over the past century: Effects on the ionosphere-thermosphere system and solar quiet (Sq) magnetic variation. *Journal of Geophysical Research: Space Physics*, *118*, 849–858. https://doi.org/10.1029/2012JA018447

de Haro Barbas, B. F., Elias, A. G., Cnossen, I., & Zossi de Artigas, M. (2013). Long-term changes in solar quiet (Sq) geomagnetic variations related to Earth's magnetic field secular variation. *Journal of Geophysical Research: Space Physics*, *118*, 3712–3718. https://doi.org/10.1002/jgra.50352

Doumbia, V., Maute, A., & Richmond, A. D. (2007). Simulation of equatorial electrojet magnetic effects with the Thermosphere-Ionosphere-Electrodynamics General Circulation Model. *Journal of Geophysical Research*, *112*, A09309. https://doi.org/10.1029/2007JA012308

Efron, B. (1981). Nonparametric estimates of standard error: The jackknife, the bootstrap, and other methods. *Biometrika*, *68*(3), 589–599. https://doi.org/10.1093/biomet/68.3.589

Elias, A. G., De Artigas, M. Z., & de Haro Barbas, B. F. (2010). Trends in the solar quiet geomagnetic field variation linked to the Earth's magnetic field secular variation and increasing concentrations of greenhouse gases. *Journal of Geophysical Research*, *115*, A08316. https://doi.org/10.1029/2009JA015136

Fang, T.-W., Akmaev, R., Fuller-Rowell, T., Wu, F., Maruyama, N., & Millward, G. (2013). Longitudinal and day-to-day variability in the ionosphere from lower atmosphere tidal forcing. *Geophysical Research Letters*, *40*, 2523–2528. https://doi.org/10.1002/grl.50550

Farquharson, C. G., & Oldenburg, D. W. (1998). Non-linear inversion using general measures of data misfit and model structure. *Geophysical Journal International*, *134*(1), 213–227. https://doi.org/10.1046/j.1365-246X.1998.00555.x

Finlay, C. C., Olsen, N., Kotsiaros, S., Gillet, N., & Tøffner-Clausen, L. (2016). Recent geomagnetic secular variation from Swarm and ground observatories as estimated in the CHAOS-6 geomagnetic field model. *Earth, Planets and Space*, *68*(1), 112. https://doi.org/10.1186/s40623-016-0486-1

Friis-Christensen, E., Luhr, H., & Hulot, G. (2006). Swarm: A constellation to study the Earth's magnetic field. *Earth, Planets and Space*, *58*(4), 351–358. https://doi.org/10.1186/BF03351933

Friis-Christensen, E., Luhr, H., Knudsen, D., & Haagmans, R. (2008). Swarm—An Earth observationmission investigating geospace. *Advances in Space Research*, *41*(1), 210–216. https://doi.org/10.1016/j.asr.2006.10.008

Gama, L. I. (1953). *Observações da amplitude diurna da componente horizontal do campo magnética na Ilha de Fernando de Noronha*, *Publicações do Observatório Magnético de Vassouras, Ministério da Educação e Cultura* (Vol. 2, pp. 1–8). Rio de Janeiro, Brasil: Observatório Nacional.

Gama, L. I. (1958). *Installation of the Tatuoca magnetic observatory*, *Publicações do Serviço Magnético, Ministério da Educação e Cultura* (Vol. 6, pp. 1–59). Rio de Janeiro, Brasil: Observatório Nacional.

Gama, L. I. (1964). *Resultados Magnéticos—Tatuoca 1959–62*, *Publicações do Serviço Magnético, Ministério da Educação e Cultura* (Vol. 12, pp. 1–169). Rio de Janeiro, Brasil: Observatório Nacional.

Gama, L. I. (1972). *Sobre a variação diurna do campo magnético no Brasil*, *Publicações de Geomagnetismo, Ministério da Educação e Cultura* (Vol. 15, pp. 1–38). Rio de Janeiro, Brasil: Observatório Nacional.

Gouin, P. (1962). Reversal of the magnetic daily variation at Addis Ababa. *Nature*, *193*(4821), 1145–1146. https://doi.org/10.1038/1931145a0

Gurubaran, S. (2002). The equatorial counter electrojet: Part of a worldwide current system? *Geophysical Research Letters*, *29*(9), 1337. https://doi.org/10.1029/2001GL014519

Hagan, M. E., & Forbes, J. M. (2002). Migrating and nonmigrating diurnal tides in the middle and upper atmosphere excited by tropospheric latent heat release. *Journal of Geophysical Research*, *107*(D24), 4754. https://doi.org/10.1029/2001JD001236

Hagan, M. E., & Forbes, J. M. (2003). Migrating and nonmigrating semidiurnal tides in the upper atmosphere excited by tropospheric latent heat release. *Journal of Geophysical Research*, *108*(A2), 1062. https://doi.org/10.1029/2002JA009466

Hamid, N. S. A., Liu, H., Uozumi, T., Yumoto, K., Veenadhari, B., Yoshikawa, A., & Sanchez, J. A. (2014). Relationship between the equatorial electrojet and global Sq currents at the dip equator region. *Earth, Planets and Space*, *66*(1), 146. https://doi.org/10.1186/s40623-014-0146-2

Hanuise, C., Mazaudier, C., Vila, P., Blanc, M., & Crochet, M. (1983). Global dynamo simulation of ionospheric currents and their connection with the equatorial electrojet and counter electrojet: A case study. *Journal of Geophysical Research*, *88*(A1), 253–270. https://doi.org/10.1029/JA088iA01p00253

Hartmann, G. A., & Pacca, I. G. (2009). Time evolution of the South Atlantic Magnetic Anomaly. *Anais da Academia Brasileira de Ciências*, *81*(2), 243–255. https://doi.org/10.1590/S0001-37652009000200010

Hesse, D. (1982). An investigation of the equatorial electrojet by means of ground based magnetic measurements in Brazil. *Annales Geophysicae*, *38*(3), 315–320.

Jankowski, J., & Sucksdorff, C. (1996). *IAGA guide for magnetic measurements and observatory practice*. Warsaw: International Association of Geomagnetism and Aeronomy.

Love, J. J. (2009). Missing data and the accuracy of magnetic-observatory hour means. *Annales Geophysicae*, *27*(9), 3601–3610. https://doi.org/10.5194/angeo-27-3601-2009

Lühr, H., Maus, S., & Rother, M. (2004). Noon-time equatorial electrojet: Its spatial features as determined by the CHAMP satellite. *Journal of Geophysical Research*, *109*, A01306. https://doi.org/10.1029/2002JA009656

Malin, S. R. C. (1970). Separation of lunar daily geomagnetic variations into parts of ionospheric and oceanic origin. *Geophysical Journal International*, *21*(5), 447–455. https://doi.org/10.1111/j.1365-246X.1970.tb01781.x

Malin, S. R. C. (1973). Worldwide distribution of geomagnetic tides. *Philosophical Transactions of the R. Society of London. Series A, Mathematical and Physical Sciences*, *274*(1243), 551–594. https://doi.org/10.1098/rsta.1973.0076

Malin, S. R. C., & Chapman, S. (1970). The determination of lunar daily geophysical variations by the Chapman-Miller method. *Geophysical Journal International*, *19*(1), 15–35. https://doi.org/10.1111/j.1365-246X.1970.tb06738.x

Mann, R. J., & Schlapp, D. M. (1988). The equatorial electrojet and the day-ato-day variability of Sq. *Journal of Atmospheric and Terrestrial Physics*, *50*(1), 57–62. https://doi.org/10.1016/0021-9169(88)90009-8

Marriott, R. T., Richmond, A. D., & Venkateswaran, S. V. (1979). The quiet-time equatorial electrojet and counter-electrojet. *Journal of Geomagnetism and Geoelectricity*, *31*(3), 311–340. https://doi.org/10.5636/jgg.31.311

Marsh, D. R., Mills, M. J., Kinnison, D. E., & Lamarque, J.-F. (2013). Climate change from 1850 to 2005 simulated in CESM1(WACCM). *Journal of Climate*, *26*(19), 7372–7391. https://doi.org/10.1175/JCLI-D-12-00558.1

Matzka, J., Chulliat, A., Mandea, M., Finlay, C. C., & Qamili, E. (2010). Geomagnetic observations for main field studies: From ground to space. *Space Science Reviews*, *155*(1–4), 29–64. https://doi.org/10.1007/s11214-010-9693-4

Matzka, J., Siddiqui, T. A., Lilienkamp, H., Stolle, C., & Veliz, O. (2017). Quantifying solar flux and geomagnetic main field influence on the equatorial ionospheric current system at the geomagnetic observatory Huancayo. *Journal of Atmospheric and Solar-Terrestrial Physics*, *163*, 120–125. https://doi.org/10.1016/j.jastp.2017.04.014

Maus, S., & Lühr, H. (2005). Signature of the quiet-time magnetospheric magnetic field and its electromagnetic induction in the rotating Earth. *Geophysical Journal International*, *162*(3), 755–763. https://doi.org/10.1111/j.1365-246X.2005.02691.x

Maus, S., Yin, F., Lühr, H., Manoj, C., Rother, M., Rauberg, J., et al. (2008). Resolution of direction of oceanic magnetic lineations by the sixth-generation lithospheric magnetic field model from CHAMP satellite magnetic measurements. *Geochemistry, Geophysics, Geosystems*, *9*, Q07021. https://doi.org/10.1029/2008GC001949

Mayaud, P. N. (1977). The equatorial counter-electrojet—A review of its geomagnetic aspects. *Journal of Atmospheric and Solar-Terrestrial Physics*, *39*(9–10), 1055–1070. https://doi.org/10.1016/0021-9169(77)90014-9

Miyahara, S., & Ooishi, M. (1997). Variation of Sq induced by atmospheric tides simulated by a middle atmosphere general circulation model. *Journal of Geomagnetism and Geoelectricity*, *49*(1), 77–87. https://doi.org/10.5636/jgg.49.77

Moro, J., Denardini, C. M., Resende, L. C. A., Chen, S. S., & Schuch, N. J. (2016). Equatorial E region electric fields at the dip equator: 2. Seasonal variabilities and effects over Brazil due to the secular variation of the magnetic equator. *Journal of Geophysical Research: Space Physics*, *121*, 10,231–10,240. https://doi.org/10.1002/2016JA022753

Morschhauser, A., Soares, G. B., Haseloff, J., Bronkalla, O., Protásio, J., Pinheiro, K., & Matzka, J. (2017). The geomagnetic observatory on Tatuoca Island, Brazil: History and recent developments. *Geoscientific Instrumentation, Methods and Data Systems*, *6*(2), 367–376. https://doi.org/10.5194/gi-6-367-2017

Olsen, J. (1951). Results of magnetic observations made at Tatuoca (Brazil) September 1933–January 1934. In *Temporary commission on the liquidation of the Polar Year 1932–33* (pp. 1–23). Copenhagen: International Meteorological Organization.

Onwumechili, C. A. (1992). Study of the return current of the equatorial electrojet. *Journal of Geomagnetism and Geoelectricity*, *44*(1), 1–42. https://doi.org/10.5636/jgg.44.1

Onwumechili, C. A. (1997). *The equatorial electrojet*. Newark: Gordon and Breach.

Onwumechili, C. A., & Ezema, P. O. (1992). Latitudinal and vertical parameters of the equatorial electrojet from an autonomous data set. *Journal of Atmospheric and Terrestrial Physics*, *54*(11–12), 1535–1544. https://doi.org/10.1016/0021-9169(92)90161-D

Qian, L., Burns, A. G., Emery, B. A., Foster, B., Lu, G., Maute, A., et al. (2014). The NCAR TIE-GCM. In J. Huba, R. Schunk, & G. Khazanov (Eds.), *Modeling the Ionosphere-Thermosphere System* (pp. 73–83). Chichester: Wiley.

Rastogi, R. G. (1974). Westward equatorial electrojet during daytime hours. *Journal of Geophysical Research*, *79*(10), 1503–1512. https://doi.org/10.1029/JA079i010p01503

Rastogi, R. G., Alex, S., & Patil, A. (1994). Seasonal variations of geomagnetic D, H and Z fields at low latitudes. *Journal of Geomagnetism and Geoelectricity*, *46*(2), 115–126. https://doi.org/10.5636/jgg.46.115

Rastogi, R. G., Chandra, H., James, M. E., Kitamura, K., & Yumoto, K. (2008). Characteristics of the equatorial electrojet current in the central region of South America. *Earth, Planets and Space*, *60*(6), 623–632. https://doi.org/10.1186/BF03353126

Rastogi, R. G., Chandra, H., & Yumuto, K. J. (2010). Equatorial electrojet in east Brazil longitudes. *Journal of Earth System Science*, *119*(4), 497–505. https://doi.org/10.1007/s12040-010-0035-4

Rastogi, R. G., & Iyer, K. N. (1976). Quiet day variation of geomagnetic H-field at low latitudes. *Journal of Geomagnetism and Geoelectricity*, *28*(6), 461–479. https://doi.org/10.5636/jgg.28.461

Rastogi, R. G., & Trivedi, N. B. (2009). Asymmetries in the equatorial electrojet around N-E Brazil sector. *Annales Geophysicae*, *27*(3), 1233–1249. https://doi.org/10.5194/angeo-27-1233-2009

Rastogi, R. G., & Yumoto, K. (2006). Equatorial electrojet in the East Brazil anomaly region. *Earth, Planets and Space*, *58*, 103–106. https://doi.org/10.1186/bf03352682

Reigber, C., Lühr, H., & Schwintzer, P. (2002). CHAMP mission status. *Advances in Space Research*, *30*(2), 129–134. https://doi.org/10.1016/S0273-1177(02)00276-4

Richmond, A. D., & Maute, A. (2014). Ionospheric electrodynamics modeling. In J. Huba, R. Schunk, & G. Khazanov (Eds.), *Modeling the Ionosphere/Thermosphere System, American Geophysics Union Monograph* (pp. 57–71). Washington, DC: American Geophysics Union.

Richmond, A. D., Ridley, E. C., & Roble, R. G. (1992). A thermosphere/ionosphere general circulation model with coupled electrodynamics. *Geophysical Research Letters*, *19*(6), 601–604. https://doi.org/10.1029/92GL00401

Richmond, A. D., & Roble, R. G. (1987). Electrodynamic effects of thermospheric winds from the NCAR thermospheric general circulation model. *Journal of Geophysical Research*, *92*(A11), 12,365–12,376. https://doi.org/10.1029/JA092iA11p12365

Rigoti, A., Chamalaun, F. H., Trivedi, N. B., & Padilha, A. (1999). Characteristics of the equatorial electrojet determined from an array of magnetometers in N-NE Brazil. *Earth, Planets and Space*, *51*(2), 115–128. https://doi.org/10.1186/BF03352216

Shume, E. B., Denardini, C. M., de Paula, E. R., & Trivedi, N. B. (2010). Variabilities of the equatorial electrojet in Brazil and Perú. *Journal of Geophysical Research*, *115*, A06306. https://doi.org/10.1029/2009JA014984

Soares, G., Yamazaki, Y., Matzka, J., Pinheiro, K., Morschhauser, A., Stolle, C., & Alken, P. (2018). Equatorial counter electrojet longitudinal and seasonal variability in the American sector. *Journal of Geophysical Research: Space Physics*, *123*, 9906–9920. https://doi.org/10.1029/2018JA025968

Soares, G. B., Matzka, J., & Pinheiro, K. (2018). *Preliminary Minute Means Geomagnetic Observatory Tatuoca (TTB), 2008 to 2017* (Vol. 1). Potsdam, Germany: Potsdam, Germany: GFZ Data Services. https://doi.org/10.5880/GFZ.2.3.2018.005

Soares, G. B., Matzka, J., Pinheiro, K., Martins, C., Morschhauser, A., Rosales, D., & Vidal, E. (2020). *Hourly mean values of the geomagnetic field horizontal component H at the Geomagnetic Observatories Tatuoca (TTB) and Huancayo (HUA), 1957 to 2019* (Vol. 1). Potsdam, Germany: GFZ Data Services. https://doi.org/10.5880/GFZ.2.3.2020.002

Soares, G. B., Yamazaki, Y., Matzka, J., Pinheiro, K., Stolle, C., Alken, P., et al. (2019). Longitudinal variability of the equatorial counter electrojet during the solar cycle 24. *Studia Geophysica et Geodaetica*, *63*(2), 304–319. https://doi.org/10.1007/s11200-018-0286-0

St. Louis, B., & INTERMAGNET Operations Committee (2011). *INTERMAGNET technical reference manual V4.5*. Ottawa, Ontario, Canada: Natural Resources Canada, Observatory Crescent.

Stening, R. J. (1995). Variations in the strength of the Sq current system. *Annales Geophysicae*, *13*(6), 627–632. https://doi.org/10.1007/s00585-995-0627-5

Takeda, M. (1996). Effects of the strength of the geomagnetic main field strength on the dynamo action in the ionosphere. *Journal of Geophysical Research*, *101*(A4), 7875–7880. https://doi.org/10.1029/95JA03807

Takeda, M. (1999). Time variation of global geomagnetic Sq field in 1964 and 1980. *Journal of Atmospheric and Terrestrial Physics*, *61*(10), 765–774. https://doi.org/10.1016/S1364-6826(99)00028-0

Takeda, M. (2013). Contribution of wind, conductivity, and geomagnetic main field to the variation in the geomagnetic Sq field. *Journal of Geophysical Research: Space Physics*, *118*, 4516–4522. https://doi.org/10.1002/jgra.50386

Tapping, K. F. (2013). The 10.7 cm solar radio flux ($F_{10.7}$). *Space Weather*, *11*, 394–406. https://doi.org/10.1002/swe.20064

Tarpley, J. D. (1973). Seasonal movement of the Sq current foci and related effects in the equatorial electrojet. *Journal of Atmospheric and Terrestrial Physics*, *35*(6), 1063–1071. https://doi.org/10.1016/0021-9169(73)90005-6

Thébault, E., Finlay, C. C., Beggan, C. D., Alken, P., Aubert, J., Barrois, O., et al. (2015). International geomagnetic reference field: The 12th generation. *Earth, Planets and Space*, *67*(1), 1, 79–19. https://doi.org/10.1186/s40623-015-0228-9

Torta, J. M., Marsal, S., Curto, J. J., & Gaya-Piqué, L. R. (2010). Behaviour of the quiet-day geomagnetic variation at Livingston Island and variability of the Sq focus position in the South American-Antarctic Peninsula region. *Earth, Planets and Space*, *62*(3), 297–307. https://doi.org/10.5047/eps.2009.11.004

Weimer, D. R. (2005). Improved ionospheric electrodynamic models and application to calculating Joule heating rates. *Journal of Geophysical Research*, *110*, A05306. https://doi.org/10.1029/2004JA010884

Wienert, K. A. (1970). *Notes on geomagnetic observatory and survey practice*. Paris: UNESCO.

Yamazaki, Y., & Kosch, M. J. (2014). Geomagnetic lunar and solar daily variations during the last 100 years. *Journal of Geophysical Research*, *119*, 6732–6744. https://doi.org/10.1002/2014JA020203

Yamazaki, Y., & Maute, A. (2017). Sq and EEJ—A review on the daily variation of the geomagnetic field caused by ionospheric dynamo currents. *Space Science Reviews*, *206*(1–4), 299–405. https://doi.org/10.1007/s11214-016-0282-z

Yamazaki, Y., Richmond, A. D., Maute, A., Liu, H.-L., Pedatella, N., & Sassi, F. (2014a). On the day-to-day variation of the equatorial electrojet during quiet periods. *Journal of Geophysical Research: Space Physics*, *119*, 6966–6980. https://doi.org/10.1002/2014JA020243

Yamazaki, Y., Richmond, A. D., Maute, A., Wu, Q., Ortland, D. A., Yoshikawa, A., et al. (2014b). Ground magnetic effects of the equatorial electrojet simulated by the TIE-GCM driven by TIMED satellite data. *Journal of Geophysical Research: Space Physics*, *119*, 3150–3161. https://doi.org/10.1002/2013JA019487

Yamazaki, Y., Yumoto, K., Cardinal, M. G., Fraser, B. J., Hattori, P., Kakinami, Y., et al. (2011). An empirical model of the quiet daily geomagnetic field variation. *Journal of Geophysical Research*, *116*, A10312. https://doi.org/10.1029/2011JA016487

Yamazaki, Y., Yumoto, K., Uozumi, T., Abe, S., Cardinal, M. G., McNamara, D., et al. (2010). Reexamination of the Sq-EEJ relationship based on extended magnetometer networks in the east Asian region. *Journal of Geophysical Research*, *115*, A09319. https://doi.org/10.1029/2010JA015339

Yizengaw, E., Moldwin, M. B., Zesta, E., Biouele, C. M., Damtie, B., Mebrahtu, A., et al. (2014). The longitudinal variability of equatorial electrojet and vertical drift velocity in the African and American sectors. *Annales Geophysicae*, *32*(3), 231–238. https://doi.org/10.5194/angeo-32-231-2014

Zhou, Y.-L., Lühr, H., & Alken, P. (2018). The sidebands of the equatorial electrojet: General characteristic of the westward currents, as deduced from CHAMP. *Journal of Geophysical Research: Space Physics*, *123*, 1457–1476. https://doi.org/10.1002/2017JA024687

Zhou, Y.-L., Lühr, H., & Xu, H.-w., & Alken, P. (2018). Comprehensive analysis of the counter equatorial electrojet: Average properties as deduced from CHAMP observations. *Journal of Geophysical Research: Space Physics*, *123*, 5159–5181. https://doi.org/10.1029/2018JA025526